JGR Solid Earth

RESEARCH ARTICLE
10.1029/2025JB032603

Geothermal Reservoir Characterization at Utah FORGE Using DAS Microseismic Imaging

Yuanyuan Ma[1], Jonathan Ajo-Franklin[1], Michal Chamarczuk[1], Xiaoyu Zhu[1], Jeremy Patterson[1], Ismael Vera Rodriguez[2], David Podrasky[2], Thomas Coleman[2], Carlos Maldaner[2], and Aleta Finnila[3]

[1]Rice University, Earth, Environmental and Planetary Sciences, Houston, TX, USA, [2]Silixa, Environment & Infrastructure, Missoula, MT, USA, [3]WSP, Redmond, WA, USA

Key Points:

- Distributed Acoustic Sensing microseismic reflection imaging enables high-resolution characterization of the geothermal reservoir structure at the Utah FORGE site
- New subsurface features are revealed beyond the limits of surface arrays, including internal geologic interfaces and natural fractures
- Time-lapse fracture imaging and integration analysis provide new insights into fracture evolution and fluid interactions

Correspondence to:
Y. Ma,
ym50@rice.edu

Citation:
Ma, Y., Ajo-Franklin, J., Chamarczuk, M., Zhu, X., Patterson, J., Rodriguez, I. V., et al. (2026). Geothermal reservoir characterization at Utah FORGE using DAS microseismic imaging. *Journal of Geophysical Research: Solid Earth*, *131*, e2025JB032603. https://doi.org/10.1029/2025JB032603

Received 13 AUG 2025
Accepted 13 DEC 2025

Author Contributions:
Conceptualization: Yuanyuan Ma, Jonathan Ajo-Franklin
Data curation: Yuanyuan Ma, Jonathan Ajo-Franklin, Michal Chamarczuk, Ismael Vera Rodriguez, David Podrasky, Thomas Coleman, Carlos Maldaner
Formal analysis: Yuanyuan Ma, Jonathan Ajo-Franklin, Michal Chamarczuk, Xiaoyu Zhu, Jeremy Patterson, Ismael Vera Rodriguez, Aleta Finnila
Funding acquisition: Jonathan Ajo-Franklin
Investigation: Yuanyuan Ma, Jeremy Patterson, Aleta Finnila
Methodology: Yuanyuan Ma
Project administration: Yuanyuan Ma, Jonathan Ajo-Franklin, David Podrasky, Thomas Coleman
Resources: Yuanyuan Ma, Jonathan Ajo-Franklin, David Podrasky, Thomas Coleman, Carlos Maldaner
Software: Yuanyuan Ma

Abstract Accurate characterization of fracture geometry and reservoir structure is essential for the successful design and development of Enhanced Geothermal Systems (EGS). Conventional surface seismic imaging often lacks the resolution to delineate hydraulic fractures at depth due to strong attenuation and limited source frequency. This study presents high-resolution imaging of the Utah FORGE site using Distributed Acoustic Sensing (DAS) recorded microseismic data during the [16A(78)-32] injection activities. We developed an imaging technique that leverages microseismic events as imaging sources, applies prestack Kirchhoff migration to each individual source, then stacks hundreds of sources to generate a 3D reflectivity volume. The imaging workflow produces a high-resolution map of the regional granitoid contact and, more importantly, reveals internal structures within the heart of the geothermal reservoir that have not been previously described. By correlating well-log data and geological evidence, we identify a low-angle interface located just below and nearly parallel to the granitoid contact. Key findings also reveal two natural fractures near the stimulation zone, visible prior to stimulation, which may accommodate the injected fluid and affect the hydraulic fracturing efficiency. Those internal structures are difficult to observe by typical surface sources since the regional granite-alluvium interface is strong and not easily penetrated by seismic waves. Time-lapse imaging of the hydraulic fracture is conducted and integrated with low-frequency DAS to construct a more comprehensive fracture geometry. In conclusion, the 3D fracture volume produced by DAS microseismic reflection imaging deepens our understanding of geothermal reservoir dynamics, potentially enhancing geothermal characterization and exploitation strategies.

Plain Language Summary This study focuses on the reservoir structure and fracture surveillance of the EGS at Utah FORGE. We used fiber-optic cables installed in deep wells to record microseismic data and monitor injection activities. By employing those microseismic sources for imaging, we were able to create a detailed 3D image of the granitoid reservoir. This approach reveals previously hidden structures, including internal layer boundaries and natural fractures, that may affect how fluid propagates underground during geothermal energy production. The results also show how hydraulic fractures created during water injection connect with natural fractures, influencing the efficiency of the geothermal system. Those features have not been well demonstrated before since the granite-alluvium interface of this region is strong and attenuates surface seismic waves. This work demonstrates how fiber-optic sensing and microseismic imaging can provide valuable insights into geothermal reservoirs and improve the design and performance of EGS.

1. Introduction

Enhanced Geothermal Systems (EGS) target hot dry rock formations where the permeability necessary for fluid circulation is not naturally sufficient and must be enhanced by inducing fractures (Glassley, 2014). By combining ultra-deep drilling methods, engineered fracture stimulation techniques—developed and widely used in the unconventional oil and gas sector—EGS has moved from conceptual vision to a series of successful demonstration projects capable of accessing deep thermal resources in a wide range of geologic settings. Recent milestones, including projects at Blue Mountain (Nevada), Cape Station (Utah) (Norbeck et al., 2024), and the Utah FORGE site (England et al., 2025), highlight the accelerating maturity of EGS technology and its growing recognition as one of the most promising renewable energy.

Supervision: Yuanyuan Ma, Jonathan Ajo-Franklin, Thomas Coleman
Validation: Yuanyuan Ma, Jonathan Ajo-Franklin, Michal Chamarczuk, Xiaoyu Zhu, Ismael Vera Rodriguez, Aleta Finnila
Visualization: Yuanyuan Ma, Jeremy Patterson
Writing – original draft: Yuanyuan Ma
Writing – review & editing: Yuanyuan Ma, Jonathan Ajo-Franklin, Michal Chamarczuk, Xiaoyu Zhu, Jeremy Patterson, Ismael Vera Rodriguez, David Podrasky, Aleta Finnila

1.1. Fracture Network Characterization at EGS

As recent EGS experiments have demonstrated the ability to generate commercially meaningful flow rates, the next critical challenge is to accurately characterize fracture geometry, connectivity, and fluid transport behavior within deep, hard rock reservoirs. Accurately locating and characterizing the fracture network is highly desirable for making key decisions on well completion design, well pad spacing, and the planning of future stimulation strategies. Furthermore, subsurface formations contain pre-existing natural discontinuities, such as joints and faults, which can significantly affect the rock conductivity and fluid flow behavior. Effective EGS hydraulic stimulation creates tensile fractures and/or reactivates pre-existing shear fractures that often reorient to favor extensional propagation under in situ stress conditions (Ye & Ghassemi, 2018). Without detailed knowledge of these subsurface features, it becomes challenging to assess reservoir behavior, ensure sustainable heat extraction, and minimize operational risks such as wellbore stability issues, fluid short-circuiting, and unanticipated seismicity.

Since EGS reservoirs are usually situated several kilometers beneath the ground surface, characterizing fracture networks in EGS reservoirs faces significant technical challenges associated with data acquisition. Borehole image logs like formation Micro-Imager (FMI) and Ultrasonic Borehole Imager (UBI) remain a primary tool for identifying natural fractures and in situ stress directions (Xing et al., 2020; Ye & Ghassemi, 2024). However, logs provide only 1D information along the wellbore and cannot resolve the full 3D extent or connectivity of fracture systems. Achieving a comprehensive 3D characterization of fracture geometry and properties demands inter-disciplinary analysis and inversion of geological, geophysical, and hydrological observations. A distributed fracture network (DFN) can be inferred by various field measurements, including microseismic monitoring (Darisma et al., 2024), seismic attributes (Wadas et al., 2023), hydraulic tomography (Römhild et al., 2024), tracer measurement data (Wu et al., 2021), and integrated thermo-hydro-mechanical (THM) modeling (Ghassemi & Ratnayake, 2025). Overall, these advances highlight the increasing need for imaging techniques that can resolve fractures in 3D at the reservoir scale.

1.2. Utah FORGE

The Utah Frontier Observatory for Research in Geothermal Energy (FORGE) site is a dedicated underground field laboratory sponsored by the US Department of Energy, for developing, testing, and accelerating break-throughs in EGS technologies and advancing the uptake of geothermal resources around the world. The Utah FORGE site offers a uniquely well-instrumented field laboratory to advance next-generation fracture characterization methods for EGS. Numerous studies by researchers at the FORGE site have focused on characterizing natural fractures within the reservoir. A combination of outcrop maps, FMI data, well logs, and core testing has been used to construct DFN models (Forbes et al., 2019; Jones et al., 2024). In parallel, multiple THM simulations (Fu et al., 2025; Tounsi et al., 2025) and tracer-based interpretations (Fredd et al., 2025) have been developed to infer DFN properties and delineate potential flow paths between the injector and producer wells. Considerable geophysical efforts have also been directed toward seismic structure imaging and velocity model development. A 3D seismic reflection survey centered on the site was conducted in 2017, revealing a continuous west-dipping alluvium-granite interface but lacking clear evidence of subvertical faults beneath the contact (Miller, 2019). Kim et al. (2023) employed S-P converted phases captured by a surface nodal array and effectively imaged the regional alluvium-granite contact. Gritto (2023) developed a representative 3D seismic velocity model for the larger FORGE area using seismic reflection and well log data to support seismic resolution analysis of the fractured reservoir. While extensive efforts have been made to improve subsurface imaging and fracture characterization in this area, resolving internal structure within the crystalline bedrock remains a significant challenge, primarily due to the limited data quality and the low imaging resolution. In particular, the regional west-dipping granite-alluvium interface of this region poses a unique obstacle, as the high reflectivity boundary attenuates the seismic energy illuminating the EGS reservoir. To overcome this limitation and improve imaging quality, the use of seismic sources positioned below the granite-alluvium contact is critical.

1.3. Microseismic Reflection Imaging

Microseismic reflection imaging is a technique that utilizes microseismic events generated during fluid injection as seismic sources to image subsurface structures. Compared with the active sources (30–60 Hz) typically used in surface seismic surveys, microseismicity can act as high-frequency sources (200 Hz) located within the heart of

the stimulated reservoir, offering the advantages of increased image resolution and the ability to reveal small-scale structures that are often not visible in surface reflection surveys. This advantage is particularly critical for deep, basement geothermal reservoirs, where seismic waves attenuate rapidly and have limited ability to penetrate the basement contact. Moreover, microseismicity is typically active during injection, making imaging feasible at the time when detailed fracture characterization is most valuable. Thus, microseismic reflection imaging can serve as an important complementary tool for delineating the stimulated fracture network. The benefits of microseismic sources for imaging are similar to the resolution advantages provided by classical crosswell reflection imaging (Harris et al., 1995) except without the need to mobilize a powerful borehole source. Previous studies have demonstrated the potential of this technique using 3C geophone arrays to delineate fractures and faults (Chavarria et al., 2003; Grechka et al., 2017; Lin & Zhang, 2016). However, the broader application of this method has been limited by the sparse spatial coverage of traditional borehole seismic sensors, making reflected phases difficult to recognize.

Recently, Distributed Acoustic Sensing (DAS) has emerged as a powerful alternative for microseismic monitoring, enabling direct surveillance of fracture extent and geometry. Unlike borehole point sensors, optical fibers can be km long and provide continuous, high spatial resolution (below 1 m) monitoring of the entire wellbore. The rich microseismic wavefields observed by DAS allow for detailed tracking of subsurface wave propagation, including the reflected phases useful for imaging. These reflected seismic waves are often more easily detected in DAS microseismic data than in geophone recordings, both through manual analysis or by automated machine learning tools (Liu et al., 2024). Several studies (Ma et al., 2023, 2024a; Stanek et al., 2022) have showcased the value of DAS microseismic reflections at several field sites and have explored their application in imaging fractures and monitoring fluid movement in unconventional reservoirs. By stacking hundreds of microseismic sources to build a large migration aperture, DAS microseismic reflection imaging creates a high-resolution 3D reflectivity volume, thus allowing the direct estimation of the fracture length and height. While the microseismic reflection approach obviously requires microseismic events to occur, the zones imaged may not be the same areas as the source locations. The approach can be used to characterize aseismic features or be used to evaluate changes in reflectivity in a time-lapse manner.

In this study, we apply a recently developed imaging method (Ma, Ajo-Franklin, Nayak, et al., 2024) to characterize hydraulic fractures and geothermal reservoir structure at the Utah FORGE Site using DAS data recorded by the FOGMORE@FORGE team. First, we document and analyze DAS microseismic data acquired during the flow test in July 2023 and during the 16A and 16B dual-well stimulation sequence in April 2024. We then apply a Kirchhoff migration-based workflow proposed by Ma, Ajo-Franklin, Nayak, et al. (2024) to generate 3D reflectivity volumes and conduct time-lapse hydraulic fracture imaging. The imaging results are further correlated with well-log data, core analysis, and geological evidence for interpretation. Using the 3D reflectivity volume, we identify several previously unmapped features, hypothesized to be pre-existing basement faults with relevance to reservoir development. Our study demonstrates the capacity of DAS-based microseismic reflection imaging to better constrain both dynamic modifications of the fracture network as well as to characterize natural features that may impact EGS flow pathways and induced seismicity risk.

2. Data Overview

2.1. Utah FORGE Geologic Setting

Utah FORGE is located near Milford in Beaver County, Utah, on the western flank of the Mineral Mountains. Geologically, the site sits on the eastern edge of the narrow N/S trending Milford Basin with a maximum depth to the west of approximately 3.1 km. Figure 1 shows the geologic cross-section of the Utah FORGE Site along the trajectory of the injection-production doublet, showing well tracks, lithologies, and the temperature gradient in the reservoir (Jones et al., 2024). Near-surface cover consists of Tertiary and Quaternary alluvial deposits above interbedded claystones and tuffs (Allis et al., 2016; Jones et al., 2024; Knudsen et al., 2019). The rhyolite lies at the bottom of the basin fill, directly above the sheared top of the granitoid (Figure 1); both units thicken to the west and thin toward the east. The underlying crystalline basement rocks are dominated by hot (175°C) granites and diorites, which form a relatively homogeneous unit (Jones et al., 2024). The Opal Mound fault and the Roosevelt Hot Springs hydrothermal systems are located east of the FORGE site. At Utah FORGE, the EGS reservoir exhibits very low porosity and permeability; there is no evidence of modern hydrothermal fluid transport. The maximum horizontal stress orientation at Utah FORGE is predominantly NNE inferred from multiple data sets,

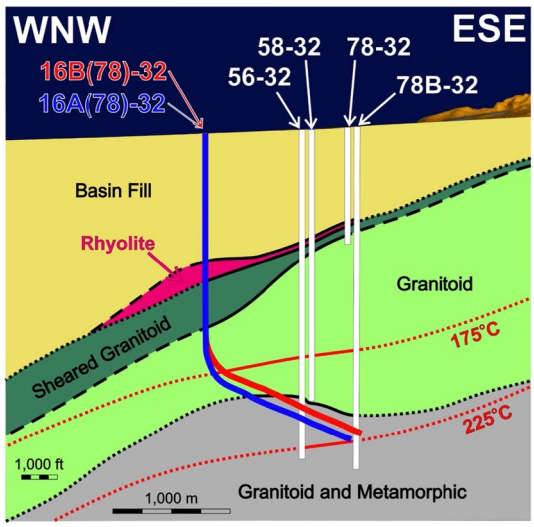

Figure 1. Geologic cross-section of the Utah FORGE Site along the trajectory of the injection-production doublet showing well tracks, lithologies, and the temperature gradient in the reservoir (figure from Jones et al., 2024).

with minor variations across different injection cycles (Xing et al., 2020, 2022; Ye & Ghassemi, 2024). This orientation is consistent with the tectonic setting: Utah FORGE lies within the southeastern Basin and Range province, where east–west extension generates north to NNE basin-bounding normal faults (Jones et al., 2024). However, recent breakout and stress analysis also indicate the possibility of strike-slip regimes (Xing et al., 2022).

The FORGE site is highly instrumented, enabling experimentation with a range of EGS monitoring techniques. The most significant EGS trial at the site to date was a sequence of stimulation and circulation tests on two deep (2,590 m) horizontally deviated wells, 16A(78)-32 (injector) and 16B(78)-32 (producer). To monitor the subsurface activities and characterize the connection between two wells, the Fiber Optic Geophysical Monitoring of Reservoir Evolution (FOGMORE@FORGE) project deployed a comprehensive suite of distributed fiber optic sensing (DFOS) systems in well 16B, including distributed acoustic, temperature, and strain sensing (DAS, DTS, and DSS, respectively). Other infrastructure utilized at the site includes a shallow vertical fiber (1,066 m) in well 78B-32, which extends DFOS coverage, as well as semi-permanent surface orbital vibrators deployed for time-lapse seismic monitoring. The fiber optic sensing cable was designed to survive high temperatures and has proven to be highly effective for geothermal reservoir monitoring (Ajo-Franklin et al., 2025; Vera Rodriguez et al., 2025a), enabling direct surveillance of fracture geometry with low-frequency DAS (LF-DAS) cross-well strain and microseismic monitoring. A thorough comparison of DAS and geophone for microseismic monitoring in the FORGE site was conducted in 2019 during the stimulation of well 58-32 (Lellouch et al., 2020), validating the effectiveness of DAS for geothermal monitoring. In this study, we explore an innovative use of DAS data to map fracture networks and further characterize the reservoir at the FORGE site.

2.2. FOGMORE DAS Systems

In July 2023, Utah FORGE performed a circulation test to investigate the hydraulic connection between the injector well 16A that was fractured in 2022, and the production well 16B (Figure 2). In April 2024, a commercial-scale stimulation sequence was conducted in both wells 16A and 16B to create new interwell flow paths. Well 16A was hydraulically fractured in eight different stages followed by four stages of stimulation in the production well 16B. To monitor injection activities, the FOGMORE@FORGE team utilized a permanently deployed fiber in the deviated well 16B and a modern high-performance interrogator unit (Carina, Silixa LLC) shown in Figure 2. The vertical well, 78B, had a single-mode optical fiber cemented behind the casing; DAS data on this fiber were recorded using a second IU (iDAS v.2, Silixa LLC). Both fibers (white dashed lines) are shorter than the wellbores; in the case of 16B the fiber terminates near the end of casing while in 78B the fiber was previously broken during deployment.

The fiber optic sensing systems recorded microseismic, LF-DAS, DSS, and DTS data during the circulation test and the stimulation periods. Distributed Acoustic Sensing data in both wells 16 and 78B were collected using a gauge length of 10 m and a spatial interval of 1.0 m, with a frequency sampling rate of 1,000 Hz. In addition to the Utah FORGE DAS stream, this study also incorporates DAS data from the Delano well provided by Fervo Energy. Delano well is a deep vertical monitoring well located at the Fervo Cape site, southwest of the 16A/16B well pad. The Delano DAS system consists of a permanently deployed single-mode fiber interrogated using a similar IU (iDAS v.2, Silixa LLC). During the FORGE stimulation sequence, Delano was operated with the same gauge length and sampling rate as the 16 and 78B systems; however, its channel spacing was greater (2 m). The availability of three wells provided improved azimuthal and depth constraints on recorded microseismic events.

2.3. DAS Microseismic Reflections

This study focuses on subsurface imaging and mainly uses the DAS microseismic data from wells 16B and Delano. The raw DAS microseismic data acquired during the circulation (Vera Rodriguez et al., 2024) and stimulation sequences were processed for hypocenter locations and moment magnitudes, steps described in prior

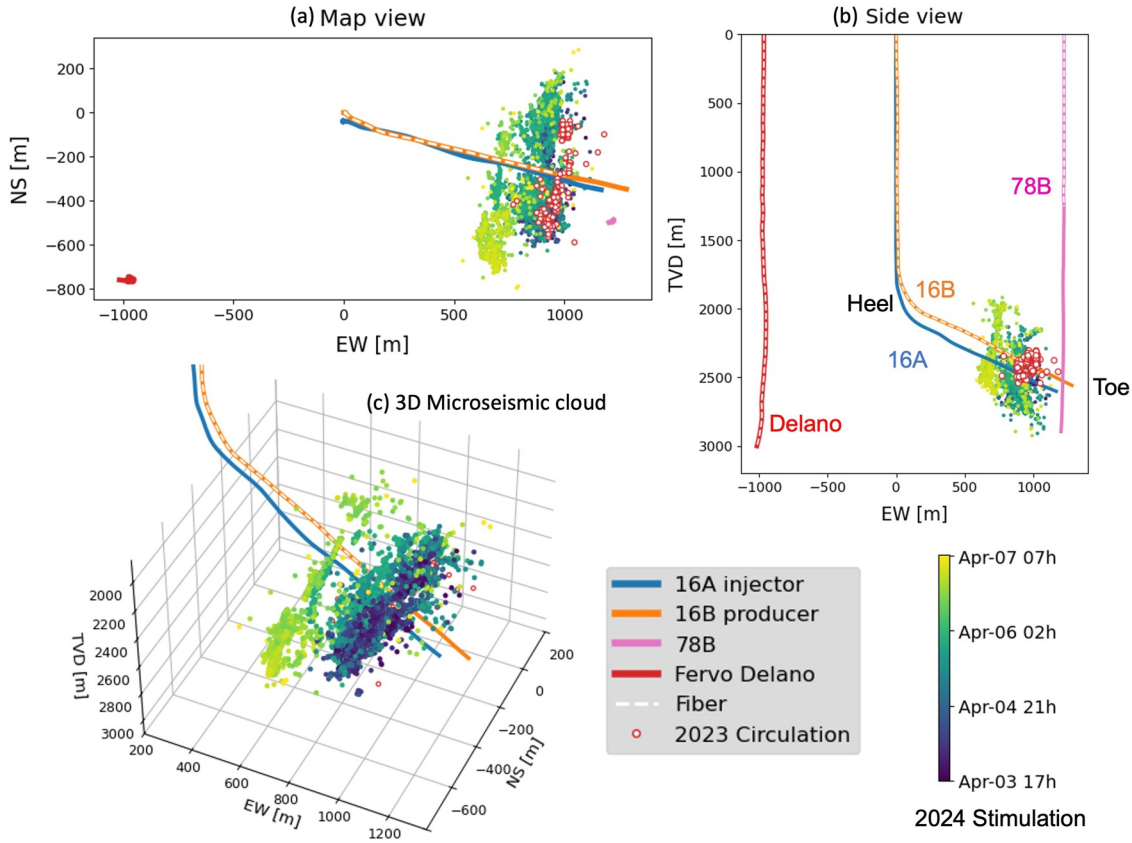

Figure 2. Well geometry at the Utah Forge site and the Fervo Cape site. (a) Map view (b) side view (c) 3D visualization. Optical fibers are permanently installed in the deviated well 16B, the vertical well 78B, and the Fervo Delano well. Microseismic clouds recorded during the circulation test in July 2023 (red circles) and the stimulation of well 16A in April 2024 (colored by origin time) are shown. The red circles in (c) appear less visible as they are located behind the 2024 stimulation, which generated a wider distribution of microseismic events.

studies (Vera Rodriguez et al., 2025a). Thousands of microseismic events were located with a calibrated 3D velocity model, revealing multiple fracture planes that were created and/or activated during stimulation activities. Figure 2 displays hypocenters of microseismicity detected during the 2023 circulation (red circles) and the 2024 stimulation of well 16A (colored by origin time).

Figure 3 presents representative microseismic events recorded by the optical fibers in well 16B and Delano. In addition to direct P- and S-wave arrivals, the microseismic wavefields exhibit abundant reflected S-waves with linear moveout and strong amplitude, which indicates the presence of nearby induced fractures or structure with sharp velocity contrasts (Ma, Ajo-Franklin, Nayak, et al., 2024). During the circulation test in July 2023 (prior to stimulation), the microseismic wavefield (Figure 3a) shows that most of the reflections (blue arrows, right dipping) propagate toward the toe side (well end). These reflections are inferred to reveal either pre-existing natural fractures or geologic structure, as at that time, only three stages were simulated in 2022 at the very end of well 16A (McLennan et al., 2023). The area where the seismic wave reflected, that is, where the reflections intersect with directions in the microseismic wavefield, has not been stimulated, excluding the possibility that these reflections are related to hydraulic fractures. The S-to-P converted phase at the top of the granite-alluvium contact (approximately 1.25 km measured depth) is clearly visible and tracked even above the granite contact; phase identification is enhanced by the dense spatial resolution provided by DAS. Those converted phases have been commonly observed in prior stimulation sequences by borehole DAS (Lellouch et al., 2020) and surface arrays (Kim et al., 2023). Figure 3b shows an event recorded by well 16B during well 16A stage 8, where three new groups of left-dipping reflected S-waves propagating toward the heel side are captured (red arrows). They are absent in the circulation wavefield and are likely generated by new hydraulic fractures created during well 16A operations, as the reservoir was stimulated only on the toe side. In a stage 9 microseismic event (Figure 3c), four such groups of left-dipping reflections are observed at the same channels, suggesting that time-lapse changes in

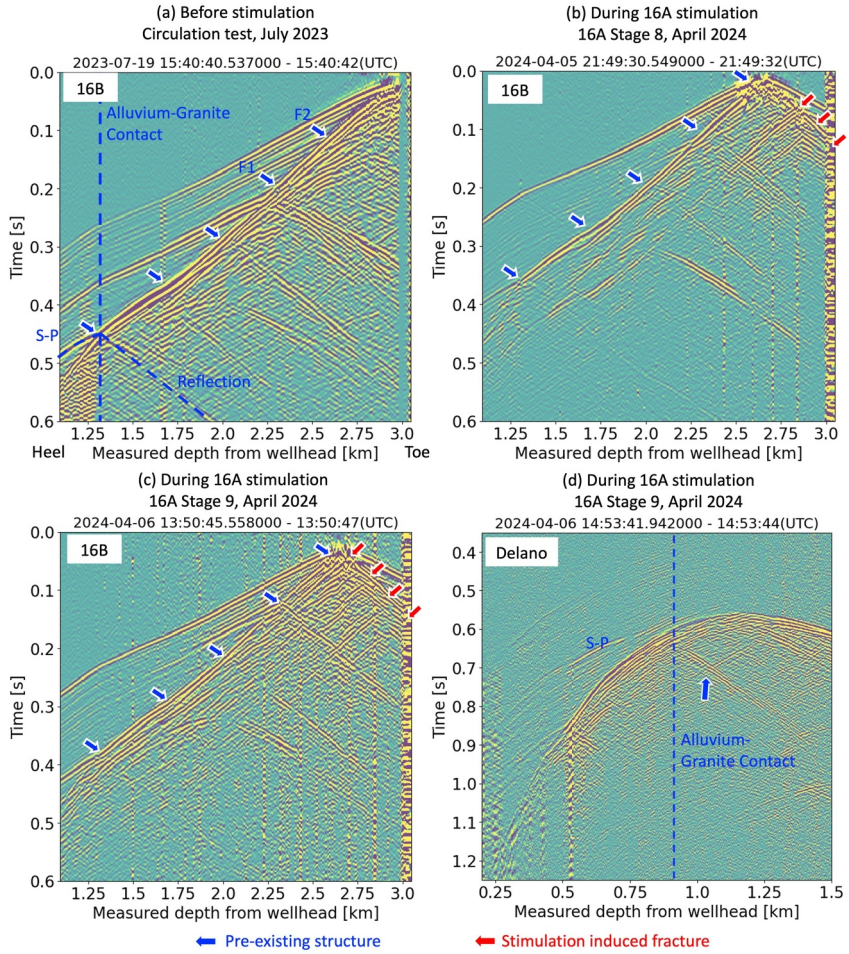

Figure 3. Examples of microseismic data recorded by the FOGMORE fiber in well 16B during (a) the circulation test in July 2023, (b) the 16A stimulation stage 8, and (c) the 16A stimulation stage 9 in April 2024. (d) One stage 9 microseismic event recorded by Delano fiber. Blue arrows indicate reflected S-waves potentially originating from pre-existing subsurface structure, while red arrows highlight reflected S-waves associated with hydraulic fractures induced by the 16A stimulation sequence in April 2024.

the hydraulic fracture set are detectable. Figure 3d shows a microseismic example during stage 9 recorded by the Delano well; despite the fact that these microseismic sources are km away from the Delano fiber, the reflected S-waves and S-P conversions on the alluvium-granite contact are still clearly identified. Integrating data from the Delano well significantly improves subsurface illumination and imaging aperture, especially for regional-scale interfaces.

Distributed Acoustic Sensing data during the well 16B stimulation are also processed. However, they are not included in this analysis as the microseismic events are less numerous and harder to detect due to in-well noise and fiber damage (Vera Rodriguez et al., 2025a). While reflected P-waves are occasionally visible in some events, this study focuses on reflected S-phases for imaging subsurface structure and fracture as they are more commonly observed and have superior data quality.

3. Methods

Before the imaging process, event selection is necessary to mitigate the potential impact of high noise levels in low signal-to-noise ratio (S/N) events on the final image quality. After analyzing the microseismic catalog (Vera Rodriguez et al., 2025c, 2025d), hypocenter uncertainties, and data quality, we selected 1,700 events that exhibit imageable reflected S-waves on the DAS data. The event selection process only excludes sources with relatively weak reflections that are obscured by noise, thereby sacrificing data quantity for better image quality. However,

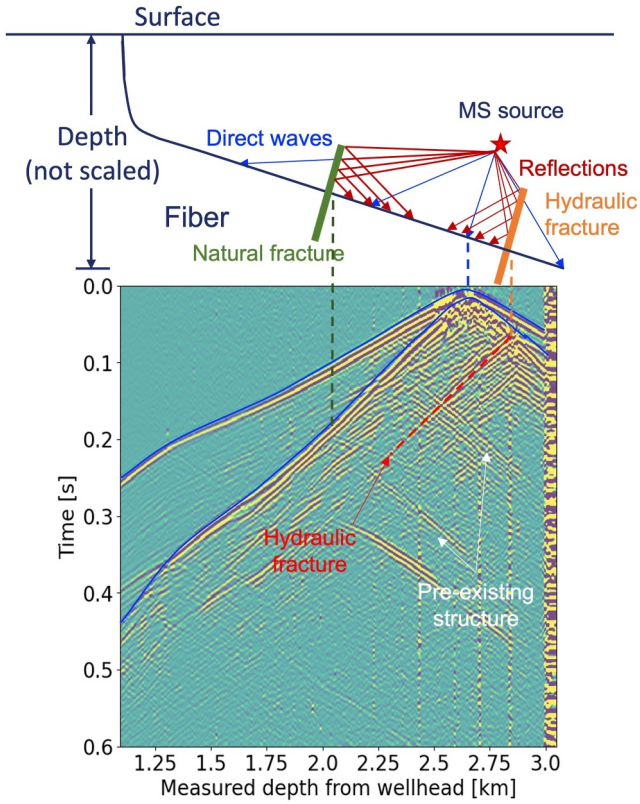

Figure 4. Schematic demonstrating the underlying concept of Distributed Acoustic Sensing (DAS) microseismic reflection imaging. Top: schematic diagram of microseismic source, receiver fiber, fracture geometry, and the ray paths. Ray paths of direct waves are shown in blue, and reflections are shown in red. Bottom: corresponding DAS microseismic gather. The consistent travel time fitting (blue) indicates a well-refined velocity model and accurate hypocenter location.

considering that the microseismic cloud is located near the injection position and illuminates a similar subsurface area, the event selection does not decrease the imaging aperture that the raw data can provide.

Figure 4 demonstrates the concept of DAS microseismic reflection imaging illustrated using the same microseismic example as shown in Figure 3b. The blue lines represent the ray path of direct waves from a microseismic event. Assuming a hydraulic fracture (orange) that is close to orthogonal to the monitoring fiber, seismic waves emitted by nearby microseismic sources travel along the red ray paths, reflect on nearby fractures, and are then recorded in the borehole. Since stimulation typically begins at the toe of the well and proceeds toward the heel, the left-dipping reflections (red dashed lines) primarily indicate hydraulic fractures in our case. In contrast, right-dipping reflections (white arrows) likely originate from pre-existing structures (green natural fracture), as the corresponding region was not stimulated at the time of recording. Thus, microseismic reflections can be used not only to image subsurface structures but also to distinguish between natural and hydraulic fractures.

Figure 5 demonstrates the workflow of the DAS microseismic reflection imaging, highlighting the key processing steps implemented in this study. The imaging strategy used in this study is to treat each microseismic event as a high-frequency seismic source, consider each fiber channel as a receiver, and apply a pre-stack Kirchhoff migration method to each individual microseismic source after wavefield separation, and then stack all sources together to build the final subsurface image volume.

The preprocessing of DAS microseismic data includes detrending, a median filter to attenuate common-mode noise, and a bandpass filter between 10 and 150 Hz. Before migration, we apply an *f-k* filter for wavefield separation and mute the direct waves to extract reflected S-waves from the raw DAS data. Conventional 3D pre-stack Kirchhoff migration is then applied separately to the wavefields propagating toward the toe and toward the heel of the lateral. We use a calibrated 3D S-wave velocity model (Vera Rodriguez et al., 2025a) to compute traveltime tables, then migrate microseismic traces on a $10 \times 10 \times 10$ m grid and output a 3D volume of potential reflectors. The grid size is chosen by considering the source location uncertainty (13.8 m), the mean shear velocity of the granite reservoir (3,400 km/s), and the

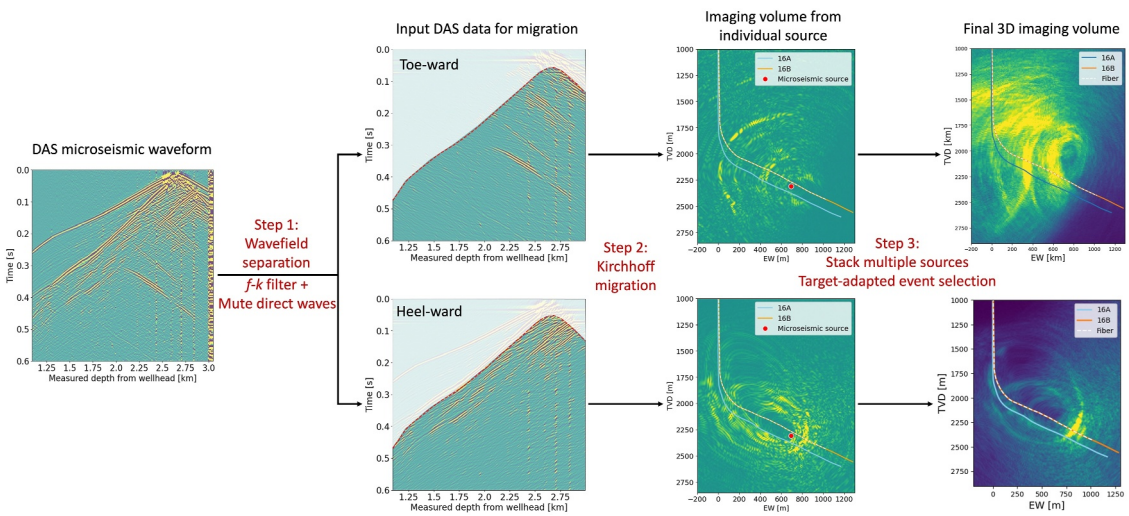

Figure 5. Overview of the Distributed Acoustic Sensing microseismic reflection imaging workflow, from wavefield separation to target-adapted stacking.

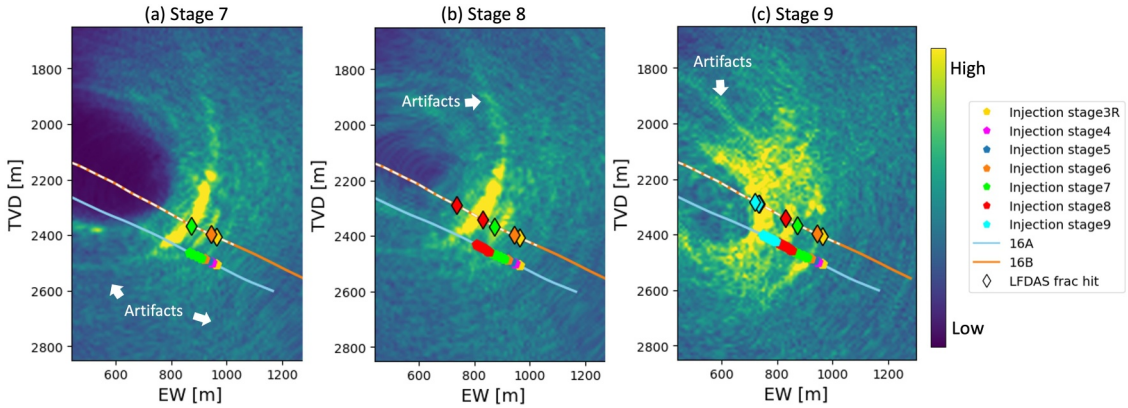

Figure 6. Time-lapse imaging of hydraulic fractures from stage 7 to stage 9 of well 16A stimulation. Blue diamonds indicate fracture hits determined using LF-DAS.

frequency filter applied to DAS microseismic data (150 Hz). After imaging individual sources, reflectors from heel-ward wavefield are stacked to map hydraulic fractures and those from toe-ward wavefield are stacked to mainly characterize pre-existing structures. Selected events for stacking are determined based on the imaging target, as the geometry of microseismic sources is unevenly distributed and different sources may illuminate different parts of the reservoir. The final output (right column in Figure 5) is a proxy for subsurface reflectivity, obtained by stacking the normalized absolute DAS fiber strain responses from multiple sources. Although it is not true reflectivity, higher amplitude values (shown in yellow) highlight locations with stronger coherent energy, indicating a high likelihood of fractures or other geological reflectors. More details of the imaging method were outlined by Ma, Ajo-Franklin, Nayak, et al. (2024).

4. Results

4.1. Time-Lapse Hydraulic Fracture Imaging

One major objective of DAS microseismic reflection imaging is to characterize the fracture network induced by stimulation and monitor fluid propagation. Figure 6 shows the side view of the imaging results with a focus on the toe side. The time-lapse images are generated by migrating only heel-ward reflections (marked by red arrows in Figure 3b) and stacking multiple microseismic sources stage by stage. Since Figure 6 does not stack all available microseismic events; instead, each image is generated using only a limited number of events occurring within that specific stage. Consequently, the apparent dipping angles of fractures are less reliable than those in the final stacked imaging results. The stacking strategy by stage is chosen to highlight how reflections evolve and to demonstrate the potential for dynamically monitoring fracture generation as the stimulation activities continue. In addition to the microseismic monitoring, the FOGMORE DAS system also recorded LF-DAS strain data for crosswell strain monitoring. When a hydraulic fracture approaches a DAS fiber, the stress at the fracture tip deforms the surrounding rock, creating a distinctive strain pattern on the waterfall plot. An approaching hydraulic fracture typically exhibits a heart-shaped extensional strain surrounded by compressional strain. This signature represents a frac hit, also known as fracture-driven interaction (Jin & Roy, 2017; Zhang et al., 2020). The frac hits (diamonds) interpreted from LF-DAS data and the perforation location of well 16A stimulation sequences are marked and colored by stage in Figure 6.

Although certain imaging artifacts (white arrows in Figure 6) are visible due to a very narrow migration aperture provided by the geometry, the imaging results show reflections from the induced fractures, consistent with the fracture intersections identified on LF-DAS. Comparing the imaging results of stage 7, 8, and 9 in Figure 6, hydraulic fractures are observed to initiate and propagate from the toe to the heel as injection activities progress. The red dashed line is a qualitative structural interpretation of fractures derived by jointly considering the reflection-imaging results and the spatial distribution of the microseismic cloud. Fractures from earlier stages remain visible in the imaging of the current stimulation stage, indicating that the fractures stay open and conductive, as the visibility of reflections requires a sufficient impedance contrast provided by fluid-filled fractures. For example, the reflectors from stage 7 appear relatively weaker than the new reflector generated in stage 8 but remain visible (Figure 6b). Similarly, the reflector from stage 6 is visible in the imaging results of

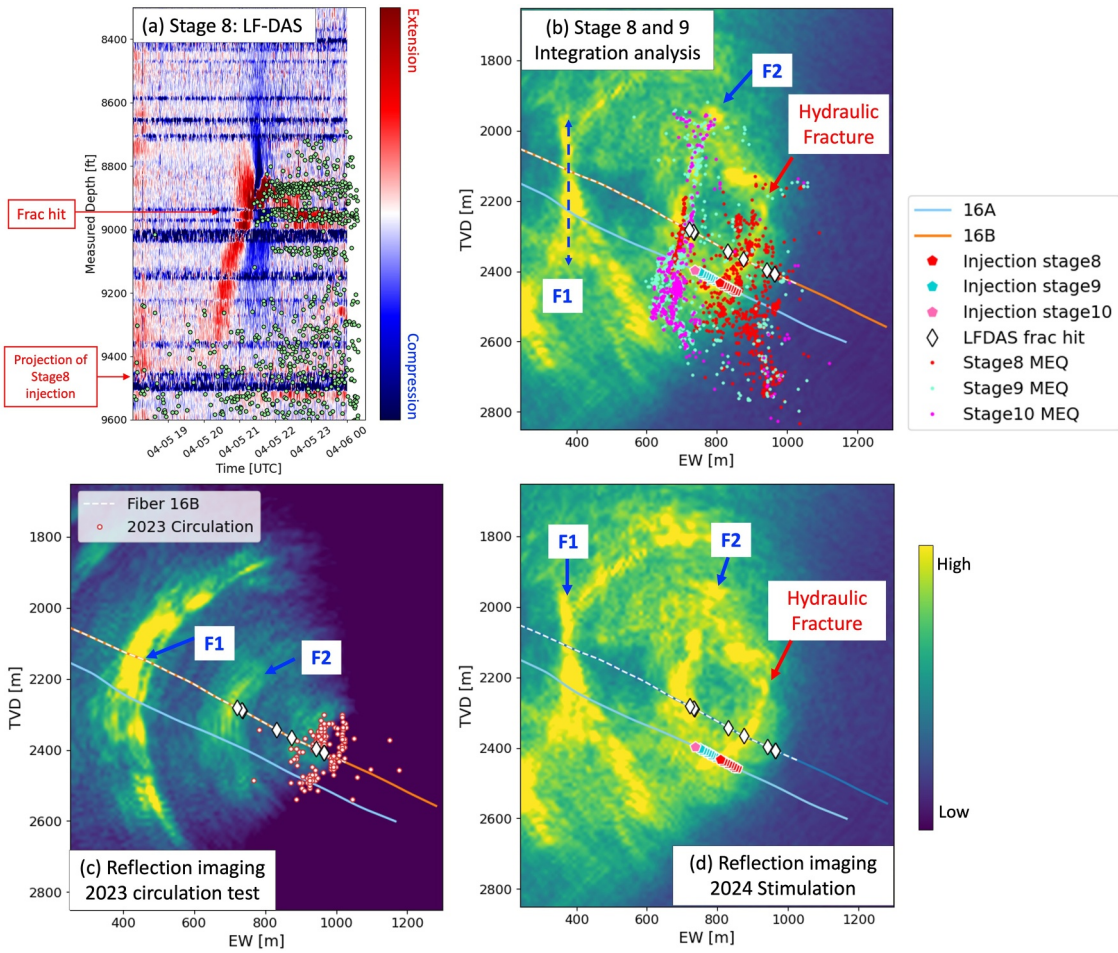

Figure 7. Integration of reflection imaging with MS cloud and LF-DAS to understand geothermal response, showing pre-existing structures affect fluid propagation. (a) LF-DAS data from stage 8 (b) Internal structure and hydraulic fracture imaged by microseismic reflections during 16A stage 8 and stage 9. (c) Reflection imaging using Distributed Acoustic Sensing data of the 2023 circulation test. (d) The same imaging results as shown in panel (b) but without the microseismic overlay, providing a cleaner view of the structural features.

stage 7 (Figure 6a). Stages 3R–6 of well 16A stimulation created fracture hits at a similar measured depth near the fiber end, as evidenced by the LF-DAS data (Ajo-Franklin et al., 2025). Consequently, only one strong reflecting fracture is imaged during stages 3R–6. Figure 6c illustrates the imaging results for stage 9 with optimized event selection. While this approach sacrifices some clarity, it preserves the majority of the reflection information, allowing all reflectors from prior stages to remain visible. The westward dipping angle of the imaged hydraulic fractures, especially in stage 7, 8, and 9, suggests that fluid propagation is influenced not only by the local stress field but also by pre-existing natural features. This aspect will be explored further in the following sections.

4.2. Natural Fracture Connections

Although the granitoid geothermal reservoir at Utah FORGE has been generally considered relatively homogeneous, recent evidence suggests that natural fractures or fault structures exist within it and may influence the reservoir response to stimulation. Figure 7 provides an integrated analysis of stages 8 and 9, showing a case where pre-existing natural fractures may affect the fluid path and fracture geometry.

To better understand the subsurface structure and the mechanism behind fracture propagation, we merged the reflection imaging results of stages 8 and stage 9, and superimposed the microseismic clouds, LF-DAS data, and injection data, as shown in Figure 7. The LF-DAS data recorded by well 16B during stage 8 stimulation is displayed in Figure 7a, with the projected injection position and the observed frac hit clearly marked. Cross-well strain data revealed that fluid propagates upward over 200 m, creating a heart-shaped "fracture" opening response

and triggering intense microseismic activity. Because hydraulic fractures typically generate fracture hits at the monitoring well near the injection depth, this upward-propagating pattern strongly suggests that a pre-existing natural fracture or fault may be influencing and accommodating the injected fluid.

Figure 7b shows the reflection imaging results with microseismic overlaid, revealing the exist of both hydraulic and natural fractures. The hydraulic fracture generated by stage 8 injection (the red dashed line in Figure 7b) is mapped by reflection imaging aligning with the microseismic clouds and the frac hit (cyan diamond). More importantly, two natural fractures (blue arrows, F1 and F2) are imaged on the west side. Both natural fractures (F1 and F2) are also visible in the 2023 circulation DAS data as shown in Figure 7c, which was acquired more than eight months prior to the stimulation campaign. Although the imaged dip angle in this earlier data set is imprecise (Figure 7c)—due to the imaging sources (red circles) being concentrated near the end of the well and providing a limited migration aperture—both faults appear at nearly the same location as observed after stimulation. The raw microseismic wavefields recorded before stimulation in Figure 3a observe clear reflected S-waves and S-to-P converted phases from F1 and F2. This consistency supports the interpretation that both F1 and F2 are pre-existing, and the inclined fault F2 becomes more open and conductive during injection.

F2 represents a west-dipping fault (approximately 85°) located at the same position of the strong heart-shaped frac hit observed in the LF-DAS data. It is worth noting that the F2 reflector shown in Figure 7b corresponds to the same fracture labeled as S9 in Figure 4c. However, Figure 4c uses only the heel-ward wavefield from Stage 9 microseismic events for imaging. Figure 7b incorporates microseismic sources from both Stage 8 and Stage 9, providing broader illumination and producing a more reliable image of the dip angle and overall geometry of F2. The microseismic cloud further demonstrates that natural fracture F2 was initially activated during stage 8 and continued to be active through the following stage 9 and stage 10. Based on the integration analysis, two primary flow paths are developed in stage 8: one aligned with hydraulic fractures near stage 7, and the other that is likely beneath the 16A well at a depth of approximately 2500 m and dips toward the heel side before reaching the production well. Figure 7d presents the same reflection imaging results shown in Figure 7b but without the microseismic overlay, providing a cleaner view of the structural features. The results indicate a possible low-angle connector linking the hydraulic fracture to F2, acting as a pathway for injected-fluid transfer.

Farther west of F2, a near-vertical natural fracture is identified through reflection imaging (labeled F1 in Figure 7b). Before the Utah FORGE 16A stimulation campaign, a commercial stimulation was conducted at the Frisco well pad in February 2024 at Fervo Energy's Cape Station facility (Fercho et al., 2025). This operation was also recorded by the 16B fiber. As shown in Figure 7b, there are no microseismic sources on the west side of F2 near the Utah FORGE 16A/16B well pad because this region has not been stimulated. To partially compensate for this lack of illumination, we selected 50 microseismic sources near the end of the Frisco wells for imaging, where the sources are relatively close to the Utah FORGE site. These sources illuminate the natural structure near 16A/16B wells from the southwest (Figure 8b) and provide a more reliable constraint on the fault dip as shown in Figure 7b. Figure 8a shows one example of Frisco microseismic events recorded by the DAS fiber in well 16B. Although the associated microseismicity did not originate near the 16A/16B well pad and the end of the 16B fiber was noisy due to operational issues (Ajo-Franklin et al., 2025), reflections from this vertical fault (F1) were still visible in the 16B DAS microseismic data (Figure 8a). Reflections from F2 are visible occasionally on Frisco microseismic sources but not reliable for imaging due to the limited data quality. Consequently, the available microseismic sources primarily improve the constraints on F1, while their contribution to imaging F2 remained limited. Despite not being directly activated by any stimulation activities, this fault produces strong reflections even in the circulation microseismic data (F1 in Figures 3a and 7c). Such persistent signals suggest that this vertical fault may act as a high-porosity fluid conduit and should be considered in future stimulation planning, particularly if operations extend toward the heel of 16A.

4.3. Regional Structure

In addition to mapping fractures, DAS microseismic reflection imaging also shows promise for revealing hidden large-scale structures at the Utah FORGE site. To obtain a more complete image of the subsurface, we also included the DAS data recorded by the Delano well (courtesy of Fervo Energy) during the 16A stimulation activities, performed reflection imaging, and combined these results with the imaging from well 16B. Reflection imaging was performed separately using the Delano and 16B data sets, and the results were subsequently merged

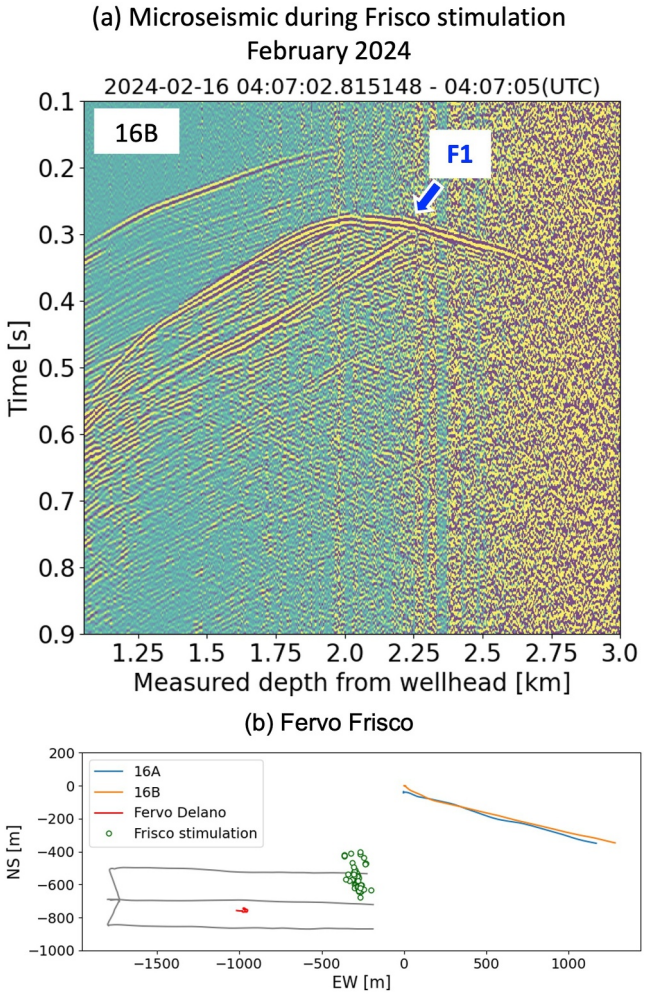

Figure 8. (a) Distributed Acoustic Sensing microseismic example recorded by the FOGMORE fiber in well 16B during the Fervo Frisco stimulation activities in February 2024 (Fercho et al., 2025). (b) Map view of the Fervo Frisco well pad.

with equal weighting after normalization. While this approach is not optimal for quantitative amplitude analysis, it is intended to preserve more structural details.

Figure 9a shows the side view of the merged image volume, presenting the regional alluvium-granite interface inferred by the imaged reflector, which is consistent with the velocity model estimated by surface nodal array studies (Zhang & Pankow, 2021) and the structure imaged by converted phases (Kim et al., 2023) but provides a higher resolution. Below the interface, two gently dipping reflectors are imaged (L1 and L2) and show similar dips as the granite contact. The regional westward-dipping basement contact hypothetically represents an abandoned, basin-bounding normal fault. Uplift and exhumation have induced widespread fracturing in basement rocks. Among fracturing orientations identified near the Utah FORGE site, most of the sheared joints strike ~180 ± 30° and dip 30° ± 30° toward the west (Bartley, 2019). This pattern may explain the imaged L1 and L2 as structures that are possibly initiated by sheared joints. Lithology and mineralogy changes within the granite basement may also contribute to those internal interfaces (Jones et al., 2024; Ma, Ajo-Franklin, Chamarczuk, et al., 2024).

Figure 9b shows the map view of the merged imaging volume, overlying the Mineral Mountain West Fault Zone (MMWFZ, Knudsen et al., 2019). The maximum horizontal stress at Utah FORGE spans between N5°E and N30°E, according to the interpretation of drilling-induced fractures and borehole image logs in 16A well (Ye & Ghassemi, 2024). The two pre-existing faults have similar NNE orientations: F1 strikes N5°E and F2 strikes N10°E approximately, aligning with the local stress field. These structural and stress orientations are consistent with the regional Basin and Range extensional setting, where the crust is undergoing east-west extension and faults typically develop as steeply dipping, north–south to NNE structures. The alignment between the imaged faults and the regional maximum horizontal stress direction indicates that the MMWFZ system may extend into basement rocks where it could interact with the hydrothermal system, however further independent analysis is required to validate the hypothesis.

From shallow to deep, the intersection depths of imaged structure have been picked and are listed in Table 1, including the granitoid contact, two internal interfaces (L1 and L2), and the two aforementioned faults (F1 and F2). Those internal structures were not previously imaged by surface seismic surveys since the granite contact of this region has a very high impedance contrast and is not easily "penetrated" by seismic waves. High-resolution imaging of those internal structures could provide insight into the understanding of the EGS reservoir and optimize stimulation and production.

5. Discussion

5.1. Well Log Analysis of Imaged Geological Structure

While the prior sections clearly demonstrate the presence of coherent seismic reflectors deep within the basement section, ambiguity remains as to the identity of these features and what further property information might be inferred. To answer this question, we further evaluated wireline and image logs acquired in well 16B with a focus on zones corresponding to the reflectors denoted as L1/L2/F1/F2. The well-log and geological data were analyzed independently from the DAS microseismic imaging results. Both L2 and F1 exhibited distinct log signatures, mainly zones of lower velocity, as measured by dipole sonic, and higher neutron porosity, as would be expected in a fault damage zone. Figures 10b and 10c, show the log signatures of L2 (top) and F1 (bottom) in black. The same intervals had distinct zones of fracturing and "rubbelization" observed using imaging logs, mainly ultrasonic borehole imaging (UBI, Figures 10d and 10e) and FMI (not shown). The velocity reductions were significant, as

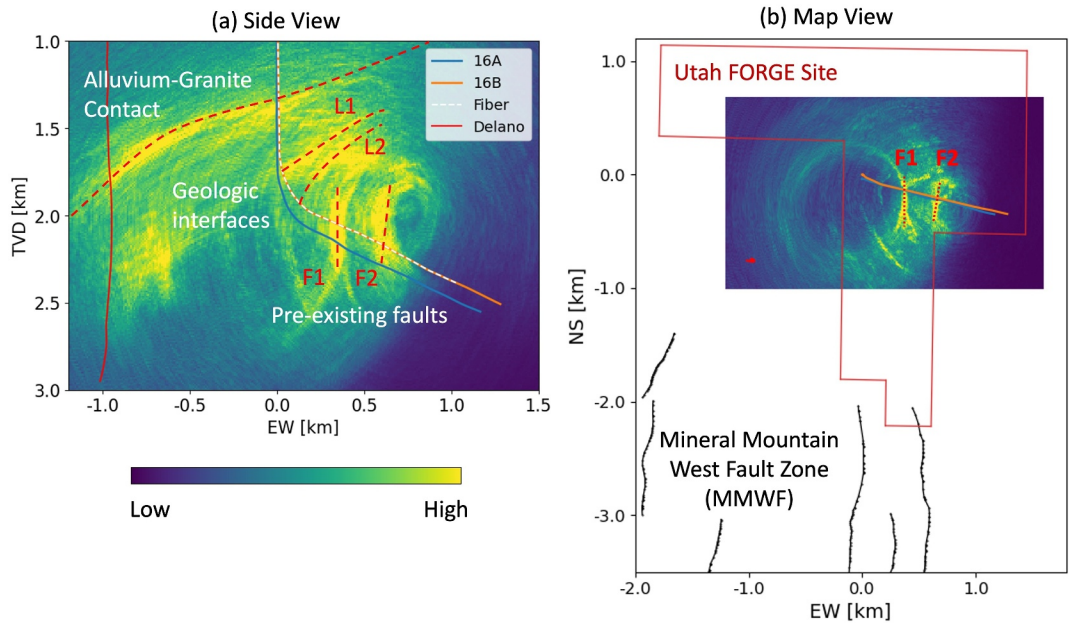

Figure 9. (a) Side view: Internal structure at Utah FORGE revealed by Distributed Acoustic Sensing microseismic reflection imaging, including the regional alluvium-granite contact, the internal interfaces, and potential fault zones. (b) Map view: Reflection imaging integrated with the regional fault map.

much as ~2000 m/s for the zone near F1, suggesting a considerably higher density of open micro fractures. Consistent with this, neutron porosities of up to 15% were observed in this same zone.

To better evaluate the relationship between mechanical damage, as evidenced by reduced Vp and versus values, and increased porosity, we conducted rock physics analysis using a Differential Effective Medium (DEM) model as described in Berryman (1992) and more recently in Mavko et al. (2020). In the DEM approach, an initially homogenous background elastic medium is perturbed through the sequential addition of inclusions, calculated by solution of a pair of coupled ordinary differential equations. In the model, an inclusion shape and moduli are required; the DEM approach has been shown to be more stable for higher inclusion fractions (Berryman, 1992). We started our analysis by calculating background elastic moduli for the zones near L2 and F1 by averaging the sonic properties in areas with low (<1%) porosity and utilizing density logs from the same regions. We assume that the inclusions are brine-filled and calculate appropriate fluid moduli using a classical empirical model (Batzle & Wang, 1992), with hydrostatic pressures (~18 MPa) and temperatures determined from DTS measurements (~200°C). We then executed DEM calculations for the range of porosities observed in the sonic logs, assuming different inclusion aspect ratios. Figure 10a shows a velocity/porosity crossplot for the F1 and L2 regions, including the results of these calculations with the best-fit inclusion aspect ratio (0.15). Note that for Vp (red/pink dots) and versus (blue/cyan dots) the trends are very similar for both L2 and F1. The DEM model shows an excellent fit to both trends. Although alternative aspect ratios are not shown in Figure 10, aspect ratios closer to 1 (spherical inclusions) were too stiff in comparison to field measurements and aspect ratios between 0.1 and 0.2 could be considered reasonable fits.

Table 1
Intersection Depth of the Imaged Structure With Well 16B

Structure	Intersection depth of the imaged structure with well 16B (m)
Granite contact	1,361
L1	1,825
L2	2,064
F1	2,318
F2	2,648

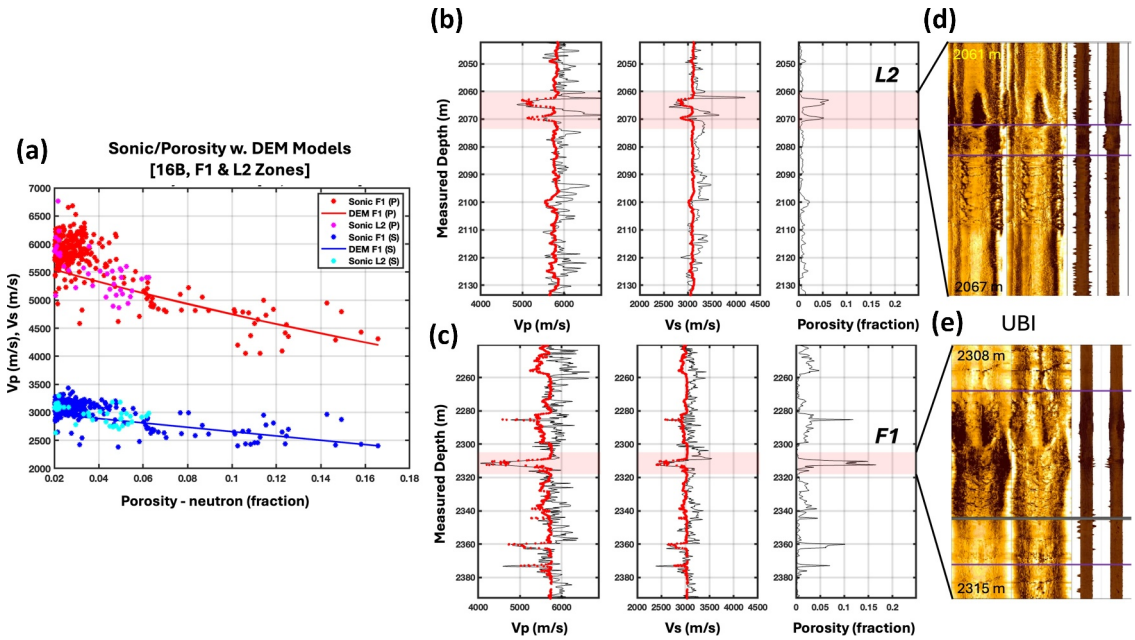

Figure 10. Wireline log and rock physics analysis of basement reflectors L2 and F1. (a) is a porosity/velocity crossplot of the zones around the L2 and F1 units. (b) and (c) are the sonic logs (left/middle) and neutron porosity logs (right) for the two units. (d) and (e) are the corresponding Ultrasonic Borehole Imager images immediately around the identified features.

While this modeling exercise demonstrates that the imaged reflections can be explained by zones of increased porosity with thin ellipsoidal cracks, the question remains as to the geologic origin of the features. One interesting aspect of both regions is a "dipole" aspect of both zones visible on neutron log with a wider symmetrical lobe spacing in L2 than F1; this observation would be consistent with damage zones flanking a small natural fault. The map view of migrated reflection data (Figure 9c) also shows that F1 and F2 are aligned with the previously characterized MMWFZ, first evaluated via surface expression to the south (Kirby, 2019; Knudsen et al., 2019) of up to 3.1 m, suggesting significant recent deformation. While the MMWFZ was not traced as far north as the Utah FORGE site, the subtle surface features utilized in initial mapping could have been removed by more recent erosion related to the Mag Lee Wash. Our present hypothesis is that F1 and F2 are small faults associated with the MMWFZ.

A secondary issue is the lack of such clear log signatures for F2, if indeed it has a similar geologic origin. While several low-angle features are visible on FMI and UBI (not shown), there is no corresponding porosity signature nor evidence of "rubbelization" on image logs. Given the measured seismic impedance and flow along this feature in Stage 8, we hypothesize that F2 is a small fault with a less cumulative slip, hence minimal zones of damage. We interpret the L1 and L2 features to be related to conjugate joint surfaces parallel and sub-parallel to the basement contact, following the geological framework proposed in Bartley (2019).

5.2. Imaging Resolution and Optimization Strategies

Several key factors influence the resolution of DAS microseismic imaging. The most fundamental factor arises from the spatial distribution of microseismic sources, which is one of the intrinsic limitations to microseismic imaging. Unlike active seismic surveys, which have specifically designed geometries to ensure multi-azimuth illumination of a particular target, microseismic events occur irregularly and only near the stimulation zone in most cases. As a result, the quality of microseismic reflection imaging is fundamentally constrained by the spatial distribution and abundance of microseismic sources. When source coverage is sparse or poorly distributed, reliable imaging becomes difficult.

The imaging results in Figure 6 exhibit curved migration artifacts caused by the narrow migration aperture provided by the source–receiver geometry. Pre-stack Kirchhoff migration sums seismic energy along the diffraction hyperbolas based on the given velocity and source-receiver geometry. In active-source imaging,

stacking multiple shots with known source wavelets generally suppresses migration artifacts because constructive and destructive interference reinforce true reflectors while canceling spurious energy. However, in our microseismic imaging workflow, the absolute waveform amplitude of multiple sources is stacked to avoid assumptions about the unknown source mechanisms and polarities of reflection phases. This prevents destructive interference from occurring, and therefore the curved migration artifacts cannot be canceled. In this study, because the microseismic sources used for migration are clustered near the fiber in 16B, they primarily illuminate the region between the sources and the fiber, leading to artifacts outside that zone. The limited coverage allows sources to illuminate only small portions of potential reflectors. As a result, geological features outside the illumination zone may exist, but the imaged dimensions, orientations, and apertures are not reliably constrained. To address this concern, limited-aperture migration or illumination analysis of each individual source-receiver pair can potentially exclude artifacts from real fracture imaging and mitigate the effect of uneven coverage (Reshetnikov et al., 2023). Similarly, incorporating multiple monitoring fibers can expand ray path coverage; for example, combining data from 16B and Fervo Delano produces a more complete structural image as shown in Figure 9.

A second key factor influencing imaging resolution is the velocity model and microseismic location uncertainty. Large location errors prevent coherent alignment of individual reflections during stacking, which can significantly smear the final stacked image and reduce the resolution. In this study, this effect is minimal because we performed careful event selection based on location uncertainty, and the excellent travel-time fits (Figure 4) indicate a well-refined velocity model and reliable hypocenters. A full simulation-based sensitivity analysis would be beneficial to quantitatively evaluate how location uncertainty affects the imaging results.

This study focuses on fracture geometrical imaging, but DAS microseismic data have the potential to recover additional fracture properties, including fracture aperture. Achieving this requires retrieving true reflection amplitudes from DAS strain measurements, which depend on careful amplitude calibration because DAS records only the axial strain-rate along the fiber. It also requires reliable event magnitude estimation to remove biases from variable source amplitude levels. Wave equation-based migration methods may provide a possible path toward true-amplitude imaging.

Although the developed imaging workflow still requires refinement and faces several technical challenges, it represents a highly promising direction for future EGS characterization. Because the method depends primarily on passive microseismicity and requires no active sources, it can be integrated into existing monitoring operations. With DAS fiber installations becoming increasingly standard in modern EGS operations, the ability to record ultra-dense microseismic wavefields provides a powerful foundation for detailed reservoir imaging. This workflow also enables long-term, continuous monitoring of reservoir evolution throughout the life of an EGS project with minimal requirement of additional field operations, as long as fiber-optic monitoring and sufficient microseismic activity are available. Furthermore, the workflow is not constrained by site-specific geology, making it inherently adaptable and offering a scalable pathway to improve fracture interpretation, refine reservoir models, and optimize stimulation design across a wide range of EGS sites and other deep reservoirs.

6. Conclusions

This study highlights the potential of DAS microseismic reflection imaging for high-resolution subsurface characterization and fracture mapping within geothermal reservoirs. By leveraging DAS and microseismic sources, the developed workflow revealed key subsurface structures at the Utah FORGE site: (a) the west-dipping regional basement contact; (b) two internal interfaces within the basement reservoir dipping parallel with the contact; (c) two natural fractures in the granitoid reservoir, one near vertical and the other one slightly inclined near the stimulation zone and affects fluid paths injected from well 16A. Distributed Acoustic Sensing microseismic imaging also facilitates the time-lapse imaging of hydraulic fractures and flow communication between the injection and production well stage by stage. We expect these findings to provide critical insights into understanding geothermal reservoir dynamics, improving EGS efficiency and sustainability, and optimizing EGS exploitation. Future work will focus on refining imaging techniques, integrating with multi-disciplinary data, and extending applications to a broader range of geothermal systems.

Conflict of Interest

The authors declare no conflicts of interest relevant to this study.

Data Availability Statement

The DAS microseismic event triggers (waveforms) recorded during the 2023 16A-16B circulation tests are available at (Vera Rodriguez et al., 2025b). The corresponding microseismic event catalog can be accessed at (Vera Rodriguez et al., 2025c). The microseismic catalog for the 2024 16A-16B dual-well stimulation is available at (Vera Rodriguez et al., 2025d), and the LF-DAS data used in this study can be accessed via (Zhu et al., 2025). The DAS microseismic event triggers of the 2024 16A-16B stimulation sequence will be uploaded to GDR in the near future (pending data set size considerations) and can currently be obtained by contacting ym50@rice.edu.

Acknowledgments
This project is supported by DOE EERE Geothermal Technologies Office to Utah FORGE and the University of Utah under Project DE-EE0007080 Enhanced Geothermal System Concept Testing and Development at the Milford City, Utah Frontier Observatory for Research in Geothermal Energy (Utah FORGE) site. We appreciate the assistance and support of the FOGMORE@Utah FORGE team, Utah FORGE project 3-2417. The authors are grateful to Fervo Energy for providing the DAS data from the Delano well and Granting permission to publish this work. We thank Dr. Clay Jones for the valuable discussions on the well log data and geological background of the Utah FORGE site, and Dr. Typer Knudsen for sharing the fault data set used in this study.

References

Ajo-Franklin, J., Chamarczuk, M., Ma, Y., Kim, J., Coleman, T., Maldaner, C., et al. (2025). Distributed fiber optic sensing deployment in a deep EGS production well at Utah FORGE: Preliminary results and lessons learned. In *Proceedings, 50th workshop on geothermal reservoir engineering*. Stanford University.

Allis, R., Moore, J., Davatzes, N., Gwynn, M., Hardwick, C., Kirby, S., et al. (2016). EGS concept testing and development at the Milford, Utah FORGE site. In *Proceedings 41st workshop on geothermal reservoir engineering*. Stanford University.

Bartley, J. M. (2019). Joint patterns in the mineral Mountains intrusive complex and their roles in subsequent deformation and magmatism. In R. Allis & J. N. Moore (Eds.), *Geothermal characteristics of the roosevelt hot springs system and adjacent FORGE EGS site* (Vol. 169-C, p. 131). Utah Geological Survey Miscellaneous Publication. https://doi.org/10.34191/MP-169-C

Batzle, M. L., & Wang, Z. (1992). Seismic properties of pore fluids. *Geophysics*, *57*(11), 1396–1408. https://doi.org/10.1190/1.1443207

Berryman, J. G. (1992). Single-scattering approximations for coefficients in Biot's equations of poroelasticity. *Journal of the Acoustical Society of America*, *91*(2), 551–571. https://doi.org/10.1121/1.402518

Chavarria, J. A., Malin, P., Catchings, R. D., & Shalev, E. (2003). A look inside the San Andreas Fault at Parkfield through vertical seismic profiling. *Science*, *302*(5651), 1746–1748. https://doi.org/10.1126/science.1090711

Darisma, D., Mukuhira, Y., Okamoto, K., Tanaka, Y., Uchide, T., Ishibashi, T., et al. (2024). Building the fracture network model for the Okuaizu geothermal field based on microseismic data analysis. *Earth Planets and Space*, *76*(1), 107. https://doi.org/10.1186/s40623-024-02049-w

England, K., Li, P. J., Xing, P., Moore, J., & McLennan, J. (2025). *Enhanced geothermal system hydraulic fracturing campaign at Utah FORGE. SPE hydraulic fracturing technology conference and exhibition*. The Woodlands. https://doi.org/10.2118/223519-MS

Fercho, S., Norbeck, J., Dadi, S., Matson, G., Borell, J., McConville, E., et al. (2025). Update on the geology, temperature, fracturing, and resource potential at the Cape geothermal project informed by data acquired from the drilling of additional horizontal EGS Wells. In *Proceedings, 50th workshop on geothermal reservoir engineering*. Stanford University.

Forbes, B., Moore, J., Finnila, A., Podgorney, R., Nadimi, S., & McIennan, J. (2019). Natural fracture characterization at the Utah FORGE EGS Test site: Discrete natural fracture network, stress field, and critical stress analysis. In *Geothermal characteristics of the roosevelt hot springs system and adjacent FORGE EGS site* (p. 169). Utah Geological Survey Miscellaneous Publication. https://doi.org/10.34191/MP-169-N

Fredd, C. N., de Cerf, C., Giri, P., Hartvig, S., Huseby, O., McLennan, J., & England, K. (2025). Advanced tracer interpretation at Utah FORGE provides new insights on completion and stimulation challenges for enhanced geothermal systems and tight formations. In *Proceedings of the 2025 Unconventional Resources Technology Conference (URTeC 2025)*. Paper URTEC-4258944-MS. https://doi.org/10.15530/urtec-2025-4258944

Fu, W., Damjanac, B., Radaković-Guzina, Z., Podgorney, R., & McLennan, J. (2025). Modeling near-wellbore fracture evolution and tortuosity at the Utah FORGE geothermal test site. In *Proceedings of the 2025 Unconventional Resources Technology Conference (URTeC 2025)*. Paper URTEC-4240554-MS. https://doi.org/10.15530/urtec-2025-4240554

Ghassemi, A., & Ratnayake, R. (2025). Hydraulic fracturing in geothermal reservoirs: The Utah FORGE EGS and Newberry superhot projects. In *SPE hydraulic fracturing technology conference and exhibition*. The Woodlands. https://doi.org/10.2118/223576-MS

Glassley, W. E. (2014). *Geothermal energy: Renewable energy and the environment* (2nd ed.). CRC Press. https://doi.org/10.1201/b17521

Grechka, V., Li, Z., Howell, B., Garcia, H., & Wooltorton, T. (2017). High-resolution microseismic imaging. *The Leading Edge*, *36*(10), 822–828. https://doi.org/10.1190/tle36100822.1

Gritto, R. (2023). Utah FORGE 3-2535: Preliminary report on development of a reservoir seismic velocity model [Dataset]. *Geothermal Data Repository*. https://gdr.openei.org/submissions/1470

Harris, J. M., Nolen-Hoeksema, R. C., Langan, R. T., Schaack, M. V., Lazaratos, S. K., & Rector, J. W. (1995). High-resolution crosswell imaging of a west Texas carbonate reservoir: Part 1—Project summary and interpretation. *Geophysics*, *60*(3), 667–681. https://doi.org/10.1190/1.1443806

Jin, G., & Roy, B. (2017). Hydraulic-fracture geometry characterization using low-frequency das signal. *The Leading Edge*, *36*(12), 975–980. https://doi.org/10.1190/tle36120975.1

Jones, C., Simmons, S., & Moore, J. (2024). Geology of the Utah frontier observatory for research in geothermal energy (FORGE) enhanced geothermal system (EGS) site. *Geothermics*, *122*, 103054. https://doi.org/10.1016/j.geothermics.2024.103054

Kim, J., Ajo-Franklin, J., Shadoan, V., Sobolevskaia, J., Correa, J., & Freifeld, B. (2023). A dense linear array for passive seismic imaging of geothermal structural features: The FOAL experiment at Utah FORGE. In *SEG International Exposition and Annual Meeting* (p. SEG-2023). SEG. https://doi.org/10.1190/image2023-3913927

Kirby, S. M. (2019). Revised mapping of bedrock geology adjoining the Utah FORGE site. In *Geothermal Characteristics of the Roosevelt Hot Springs System and Adjacent FORGE EGS Site* (Vol. 169-A, pp. 12–19). Utah Geological Survey Miscellaneous Publication. https://doi.org/10.34191/MP-169-A

Knudsen, T., Kleber, E., Hiscock, A., & Kirby, S. M. (2019). Quaternary geology of the Utah FORGE site and vicinity, Millard and Beaver Counties. In *Geothermal characteristics of the Roosevelt Hot Springs system and adjacent FORGE EGS site*. Geological Survey Miscellaneous Publication. https://doi.org/10.34191/MP-169-B

Lellouch, A., Lindsey, N. J., Ellsworth, W. L., & Biondi, B. L. (2020). Comparison between distributed acoustic sensing and geophones: Downhole microseismic monitoring of the FORGE geothermal experiment. *Seismological Research Letters*, *91*(6), 3256–3268. https://doi.org/10.1785/0220200149

Lin, Y., & Zhang, H. (2016). Imaging hydraulic fractures by microseismic migration for downhole monitoring system. *Physics of the Earth and Planetary Interiors*, *261*, 88–97. https://doi.org/10.1016/j.pepi.2016.06.010

Liu, Y., Chen Ning, I. L., & Nihei, K. (2024). *Automatic detection of DAS-Recorded microseismic fracture reflections* (pp. 543–547). SEG Technical Program Expanded Abstracts. https://doi.org/10.1190/image2024-4095418.1

Ma, Y., Ajo-Franklin, J., Chamarczuk, M., Patterson, J., Rodriguez, I. V., Podrasky, D., et al. (2024). Illuminating geothermal reservoir structure: DAS microseismic imaging at Utah FORGE. *Image*, 2024–2552. https://doi.org/10.1190/image2024-4078563.1

Ma, Y., Ajo-Franklin, J., Nayak, A., Zhu, J., Correa, J., & Kerr, E. (2024). Distributed acoustic sensing microseismic reflection imaging for hydraulic fracture and fault zones mapping. *Geophysics*, *89*(4), D183–D192. https://doi.org/10.1190/geo2023-0582.1

Ma, Y., Eaton, D., Wang, C., & Aklilu, A. (2023). Characterizing hydraulic fracture growth using distributed acoustic sensing-recorded microseismic reflections. *Geophysics*, *88*(6), WC47–WC57. https://doi.org/10.1190/geo2022-0607.1

Mavko, G., Mukerji, T., & Dvorkin, J. (2020). *The rock physics handbook* (3rd ed.). Cambridge University Press.

McLennan, J., England, K., Rose, P., Moore, J., & Barker, B. (2023). Stimulation of a high-temperature granitic reservoir at the Utah FORGE site. In *Society of petroleum engineers - SPE hydraulic fracturing technology conference and exhibition 2023, HFTC 2023*. https://doi.org/10.2118/212346-MS

Miller, J. (2019). Utah FORGE: Seismic reflection data [Dataset]. *Geothermal Data Repository. Energy and Geoscience Institute at the University of Utah*. https://doi.org/10.15121/1542059

Norbeck, J. H., Gradl, C., & Latimer, T. (2024). Deployment of enhanced geothermal system technology leads to rapid cost reductions and performance improvements. *eartharxiv*. https://doi.org/10.31223/X5VH8C

Reshetnikov, A., Nazarova, A., Taylor, S., Haffener, J., Langton, D., Biholar, A., & Sloan, A. (2023). *Observations, learnings, and validation of conductive fracture imaging: Hydraulic fracturing technology conference and exhibition, SPE*. The Woodlands.

Römhild, L., Ringel, L. M., Liu, Q., Hu, L., Ptak, T., & Bayer, P. (2024). Hybrid discrete fracture network inversion of hydraulic tomography data from a fractured-porous field site. *Water Resources Research*, *60*(1), e2023WR036035. https://doi.org/10.1029/2023WR036035

Staněk, F., Jin, G., & Simmons, J. (2022). Fracture imaging using DAS-Recorded microseismic events. *Frontiers in Earth Science*, *10*, 907749. https://doi.org/10.3389/feart.2022.907749

Tounsi, H., Damjanac, B., Radaković-Guzina, Z., Fu, W., Finnila, A., Xing, P., et al. (2025). Influence of natural fractures on hydraulic stimulation in geothermal reservoirs: Insights from Utah FORGE coupled hydro-mechanical modeling. In *Proceedings of the 2025 Unconventional Resources Technology Conference (URTeC 2025)*. Paper URTEC-4264117. https://doi.org/10.15530/urtec-2025-4264117

Vera Rodríguez, I., Coleman, T., Podrasky, D., Maldaner, C., Ma, Y., & Ajo Franklin, J. (2025). DAS moment tensor inversion analysis for microseismic events observed during the 2023 circulation tests at Utah FORGE. In *Proceedings, 50th workshop on geothermal reservoir engineering*. Stanford University.

Vera Rodriguez, I., Podrasky, D., Coleman, T., Maldaner, C., Ma, Y., & Ajo-Franklin, J. (2025b). Utah FORGE 3-2417: DAS microseismic event records from circulation test - July, 2023 [Dataset]. *Geothermal Data Repository*. https://gdr.openei.org/submissions/1747

Vera Rodriguez, I., Podrasky, D., Maldaner, C., Coleman, T., Ma, Y., & Ajo-Franklin, J. (2025d). Utah FORGE 3-2417: DAS microseismic event catalog from April 2024 stimulation [Dataset]. *Geothermal Data Repository*. https://gdr.openei.org/submissions/1744

Vera Rodriguez, I., Podrasky, D., Maldaner, C., Ma, Y., & Ajo-Franklin, J. (2025c). Utah FORGE 3-2417: DAS Microseismic Event and MT Catalog from the 16A/16B Circulation Test [Final, Relocated], 2023 [Dataset]. *Geothermal Data Repository*. https://gdr.openei.org/submissions/1739

Vera Rodríguez, I., Wolpert, J., Podrasky, D., Coleman, T., Maldaner, C., Ma, Y., et al. (2024). DAS microseismic monitoring results from the July 2023 circulation tests at the Utah FORGE geothermal underground laboratory. In *SEG/AAPG International Meeting for Applied Geoscience and Energy, IMAGE 2024*.

Wadas, S. H., Krumbholz, J. F., Shipilin, V., Krumbholz, M., Tanner, D. C., & Buness, H. (2023). Advanced seismic characterization of a geothermal carbonate reservoir – Insight into the structure and diagenesis of a reservoir in the German Molasse Basin. *Solid Earth*, *14*(8), 871–908. https://doi.org/10.5194/se-14-871-2023

Wu, H., Fu, P., Hawkins, A. J., Tang, H., & Morris, J. P. (2021). Predicting thermal performance of an enhanced geothermal system from tracer tests in a data assimilation framework. *Water Resources Research*, *57*(12), e2021WR030987. https://doi.org/10.1029/2021WR030987

Xing, P., McLennan, J., & Moore, J. (2020). In-situ stress measurements at the Utah frontier observatory for research in geothermal energy (FORGE) site. *Energies*, *13*(21), 5842. https://doi.org/10.3390/en13215842

Xing, P., Wray, A., Velez Arteaga, E. I., Finnila, A., Moore, J., Jones, C., et al. (2022). In-situ stresses and fractures inferred from image logs at Utah FORGE. In *Proceedings of the 47th workshop on geothermal reservoir engineering*. Stanford University. SGP-TR-223.

Ye, Z., & Ghassemi, A. (2018). Experimental study on injection-induced fracture propagation and coalescence for EGS stimulation. In *Proc., 43rd workshop on geothermal reservoir engineering*. Stanford Univ.

Ye, Z., & Ghassemi, A. (2024). The updated wellbore stress models for Utah FORGE. In *Proceedings of the 49th workshop on geothermal reservoir engineering*. Stanford University. 12–14 February 2024, SGP-TR-227.

Zhang, H., & Pankow, K. L. (2021). High-resolution Bayesian spatial autocorrelation (SPAC) quasi-3-D vs model of Utah FORGE site with a dense geophone array. *Geophysical Journal International*, *225*(3), 1605–1615. https://doi.org/10.1093/gji/ggab049

Zhang, Z., Fang, Z., Stefani, J., DiSiena, J., Bevc, D., Lim Chen Ning, I., et al. (2020). Modeling of fiber-optic strain responses to hydraulic fracturing. *Geophysics*, *85*(6), A45–A50. https://doi.org/10.1190/geo2020-0083.1

Zhu, R., Podrasky, D., Coleman, T., Maldaner, C., Ma, Y., & Ajo-Franklin, J. (2025). Utah FORGE 3-2417: Low frequency distributed acoustic sensing data from 16A/16B stimulation - April, 2024 [Dataset]. *Geothermal Data Repository*. https://gdr.openei.org/submissions/1749